

Rates of Strongly Lensed Tidal Disruption Events

A Comprehensive Investigation of Black Hole, Luminosity and Temperature Dependencies

E. Mamuzic^{1,2}, T. Ryu^{2,3,4}, S. H. Suyu^{1,2}, K. Szekerczes^{5,2}, S. Huber^{2,1}, L. Dai⁶, and M. Oguri^{7,8}

¹ Technical University of Munich, TUM School of Natural Sciences, Physics Department, James-Franck-Straße 1, 85748 Garching, Germany

e-mail: elias.mamuzic@tum.de

² Max Planck Institute for Astrophysics, Karl-Schwarzschild Str. 1, 85748 Garching, Germany

e-mail: emamuzic@MPA-Garching.MPG.DE

³ JILA, University of Colorado and National Institute of Standards and Technology, 440 UCB, Boulder, 80308 CO, USA

⁴ Department of Astrophysical and Planetary Sciences, 391 UCB, Boulder, 80309 CO, USA

⁵ Department of Astronomy and Astrophysics, and Institute for Gravitation and the Cosmos, Pennsylvania State University, 525 Davey Lab, 251 Pollock Road, University Park, PA 16802, USA

⁶ Department of Physics, University of Hong Kong, Pokfulam Road, Hong Kong, People's Republic of China

⁷ Center for Frontier Science, Chiba University, 1-33 Yayoicho, Inage, Chiba 263-8522, Japan

⁸ Department of Physics, Graduate School of Science, Chiba University, 1-33 Yayoicho, Inage, Chiba 263-8522, Japan

Received - ; accepted -

ABSTRACT

In the coming years, surveys such as the Rubin Observatory's Legacy Survey of Space and Time (LSST) are expected to increase the number of observed Tidal Disruption Events (TDEs) substantially. We employ Monte Carlo integration to calculate the unlensed and lensed TDE rate as a function of limiting magnitude in u , g , r , and i -bands. We investigate the impact of multiple luminosity models, black hole mass functions (BHMFs), and flare temperatures on the TDE rate. Notably, this includes a semi-analytical model, which enables the determination of the TDE temperature in terms of black hole (BH) mass. We predict the highest unlensed TDE rate to be in g -band. It ranges from 16 to 5,440 yr^{-1} $(20,000 \text{ deg}^2)^{-1}$ for the Zwicky Transient Facility (ZTF), being more consistent with the observed rate at the low end. For LSST, we expect a rate in g -band between 3,580 and 82,060 yr^{-1} $(20,000 \text{ deg}^2)^{-1}$. A higher theoretical prediction is understandable, as we do not consider observational effects such as completeness. The unlensed and lensed TDE rates are insensitive to the redshift evolution of the BHMF, even for LSST limiting magnitudes. The best band for detecting lensed TDEs is also g -band. Its predicted rates range from 0.43 to 15 yr^{-1} $(20,000 \text{ deg}^2)^{-1}$ for LSST. The scatter of predicted rates reduces when we consider the fraction of lensed TDEs; that is, a few in ten thousand TDEs will be lensed. Despite the large scatter in the rates of lensed TDEs, our comprehensive considerations of multiple models suggest that lensed TDEs will occur in the 10-year LSST lifetime, providing an exciting prospect for detecting such events. We expect the median redshift of a lensed TDE to be between 1.5 and 2. In this paper, we additionally report on lensed TDE properties, such as the BH mass and time delays.

Key words. tidal disruption event – gravitational lensing: strong – LSST

1. Introduction

When a star ventures too close to a black hole (BH), tidal forces tear it apart. We can observe such an event as a bright transient, a so-called Tidal Disruption Event (TDE; Hills 1988; Rees 1988). These events typically last one to two years for main sequence stars (e.g., Gezari 2021), but in rare cases, they can extend much longer than that (Lin et al. 2017). By analyzing TDEs, we can infer critical properties such as the mass of the BHs and the disrupted stars (e.g., Ryu et al. 2020a), as well as gain insights into BH demographics and accretion physics (e.g., Rees 1988; Gezari 2013). Understanding TDE rates and their observational characteristics is vital for detecting them in current and future surveys such as the Zwicky Transient Facility (ZTF; Wozniak et al. 2014) and the Rubin Observatory's Legacy Survey of Space and Time (LSST; Ivezić et al. 2019). Estimating the rate of TDEs across different survey depths allows for better planning of observational campaigns and the design of strategies to maxi-

mize scientific returns (e.g., Bricman & Gomboc 2020; Lin et al. 2022).

A key advancement in this study is the inclusion of lensed TDEs in our analysis. Gravitational lensing provides a powerful mechanism to magnify and detect TDEs from deep within the cosmos. Beyond enhancing detectability, lensing offers the potential to probe cosmological parameters such as the Hubble constant (Refsdal 1964) and the size of the emission region via microlensing effects, as demonstrated for active galactic nuclei (e.g., Kochanek 2004). Despite these promising applications, the abundance and characteristics of lensed TDEs remain uncertain. Addressing this gap, we calculate the lensed TDE rate for various models and assess whether these events are numerous enough to serve as a tool for future research.

In this paper, we employ Monte Carlo simulations to calculate TDE rates as a function of limiting magnitude, following the methodology of Szekerczes et al. (2024). Likewise, we generate mock catalogs to analyze the population of unlensed and lensed

TDEs. Estimating the TDE rate requires two primary components: a TDE luminosity model and the black hole mass function (BHMF). Building upon the calculations of Szekeerczes et al. (2024), in addition to the phenomenological fit model (Thomsen et al. 2022), we incorporate the full semi-analytical stream-stream collision model for TDEs (Piran et al. 2015; Ryu et al. 2020a). This model enables the determination of the TDE temperature as a function of BH mass, eliminating the need to assume a temperature. In addition to the local BHMF adopted in Szekeerczes et al. (2024), we include two more BHMFs that account for redshift dependence, enhancing the accuracy of our predictions. For lensed TDEs, we also investigate the fraction of TDEs that are lensed for the different models, leading to a more robust forecast.

The structure of the paper is as follows: In Sect. 2, we provide an overview of the relevant theoretical background, focusing on the TDE models used to calculate the TDE magnitude. We also detail our methodology for determining the unlensed TDE rate and extending it to create a mock TDE catalog. Sect. 3 presents the results for the unlensed case, analyzing the effects of various model parameters and comparing them with current observations. In Sect. 4, we shift our focus to the lensed rate, describing the creation of mock catalogs of lensed TDEs. We then explore the lensed TDE rate, the fraction of lensed events, and the parameter distributions for the source TDE, the lens, and the lens system. Finally, we summarize our findings and conclusions in Sect. 5.

2. TDE Models and Rate Derivation

2.1. Rate Integral

We follow Szekeerczes et al. (2024) in the derivation of the unlensed TDE rate integral

$$N_{\text{TDE}} = \iint \phi_{\text{BH}}(M_{\text{BH}}) \cdot \Gamma(M_{\text{BH}}) dM_{\text{BH}} \frac{dV}{dz} dz. \quad (1)$$

Here N_{TDE} is the number of TDEs per year, M_{BH} the BH mass, Γ the TDE occurrence rate per galaxy, ϕ_{BH} the BHMF, V the volume, and z the redshift. We have already changed the variable from volume to redshift using (e.g., Oguri & Marshall 2010)

$$\frac{dV}{dz} = \Omega \cdot \frac{D_L^2}{1+z} \cdot c \cdot \frac{dt}{dz}, \quad (2)$$

where Ω is the solid angle corresponding to the survey area, D_L is the luminosity distance, c the speed of light, and $dt/dz = -1/(H \cdot (1+z))$, where H is the Hubble parameter. We adopt the TDE occurrence rate

$$\frac{\Gamma(M_{\text{BH}})}{\text{yr}^{-1}} = 10^{-4.5} \cdot \left(\frac{M_{\text{BH}}}{10^6 M_{\odot}} \right)^{-0.14}. \quad (3)$$

by Pfister et al. (2020).

In addition to the redshift-independent BHMF (Gallo & Sesana 2019; Wong et al. 2022)

$$\log_{10} \left(\frac{\phi_{\text{BH}}}{\text{Mpc}^{-3} M_{\odot}^{-1}} \right) = -9.82 - 1.10 \cdot \log_{10} \left(\frac{M_{\text{BH}}}{10^7 M_{\odot}} \right) - \left(\frac{M_{\text{BH}}}{128 \cdot 10^7 M_{\odot}} \right)^{\frac{1}{\log(10)}}, \quad (4)$$

which is illustrated in the left panel of Fig. 1, we investigate two additional ones. First, we include the BHMF derived by

the TRINITY model (Zhang et al. 2023). They used a Markov Chain Monte Carlo algorithm to fit a star-formation rate to the maximum circular halo velocity relation, a BH-to-bulge mass relation, and an active BH luminosity distribution to observed data. The derived BHMF is shown in the middle panel of Fig. 1. This BHMF displays an almost uniform redshift evolution across the BH mass range. But the evolution only affects the BHMF strongly for $z \gtrsim 2$. Second, we consider a BHMF that is calculated by combining the galaxy stellar mass function (GSMF) from Davidzon et al. (2017), and the BH-to-bulge mass relation from Kormendy & Ho (2013)

$$\frac{M_{\text{BH}}}{10^9 M_{\odot}} = 0.49 \cdot \left(\frac{M_{\text{bulge}}}{10^{11} M_{\odot}} \right)^{1.16}, \quad (5)$$

with M_{bulge} as the galaxy bulge mass. Recently, it has been suggested that this relation is redshift-dependent (e.g., Shimizu et al. 2024). However, we still assume no redshift dependence because the GSMF, which is fitted in bins to the COSMOS2015 catalog (Laigle et al. 2016), already includes a strong, non-trivial redshift dependence. As illustrated in the right panel of Fig. 1, this BHMF agrees closely with the TRINITY BHMF at $z = 0$, but not for larger redshifts. From $z = 2$ onward, the high mass end decreases while the low mass end turns and increases. This is due to the extrapolation needed to reach such low BH masses. The COSMOS2015 catalog only includes data for galaxies of just below $10^{10} M_{\odot}$. This corresponds to a BH mass of $10^{7.5} M_{\odot}$, the upper end of our considered mass range. Down to a BH mass of $10^5 M_{\odot}$ is extrapolated, assuming the fitting function is still valid.

2.2. Magnitude Bounds

The limiting magnitude of the survey gives the bounds to the integral in Eq. 1. Hence, calculating the magnitude of a given TDE is essential. Following Bessell & Murphy (2012), as done in Huber et al. (2021), we calculate the magnitude in a band X ,

$$m_{\text{AB},X} = -2.5 \cdot \log_{10} \left(\frac{\int d\lambda_{\text{obs}} \lambda \cdot S_X(\lambda_{\text{obs}}) \cdot F_{\lambda_{\text{obs}}} \cdot \text{cm}^2}{\int d\lambda_{\text{obs}} S_X(\lambda_{\text{obs}}) \cdot \frac{c}{\lambda_{\text{obs}}} \cdot \text{erg}} \right) - 48.6, \quad (6)$$

where λ_{obs} is the observed wavelength and $S_X(\lambda)$ is the band transmission function. We use the same rectangular approximations of the LSST transmission functions as Szekeerczes et al. (2024). Finally, (e.g., Huber et al. 2021)

$$F_{\lambda_{\text{obs}}} = \frac{A \cdot I_{\lambda_{\text{obs}}}}{D_L^2 (1+z)} \quad (7)$$

is the observed flux for an emitting region of area A with a spatially constant emitted specific intensity $I_{\lambda_{\text{obs}}}$. We also assume the TDE to emit as a black body described by the Planck law (Planck 1901)

$$I_{\lambda_{\text{em}}} = \frac{2hc^2}{\lambda_{\text{em}}^5} \cdot \frac{1}{e^{\frac{hc}{\lambda_{\text{em}}kT}} - 1}, \quad (8)$$

where λ_{em} is the emitted wavelength, T the temperature, h the Planck constant, and k the Boltzmann constant. In addition, also the Stefan-Boltzmann law (e.g., Baehr & Kabelac 2016) applies, allowing us to rewrite the emission area

$$A = \frac{L}{4\sigma T^4} \quad (9)$$

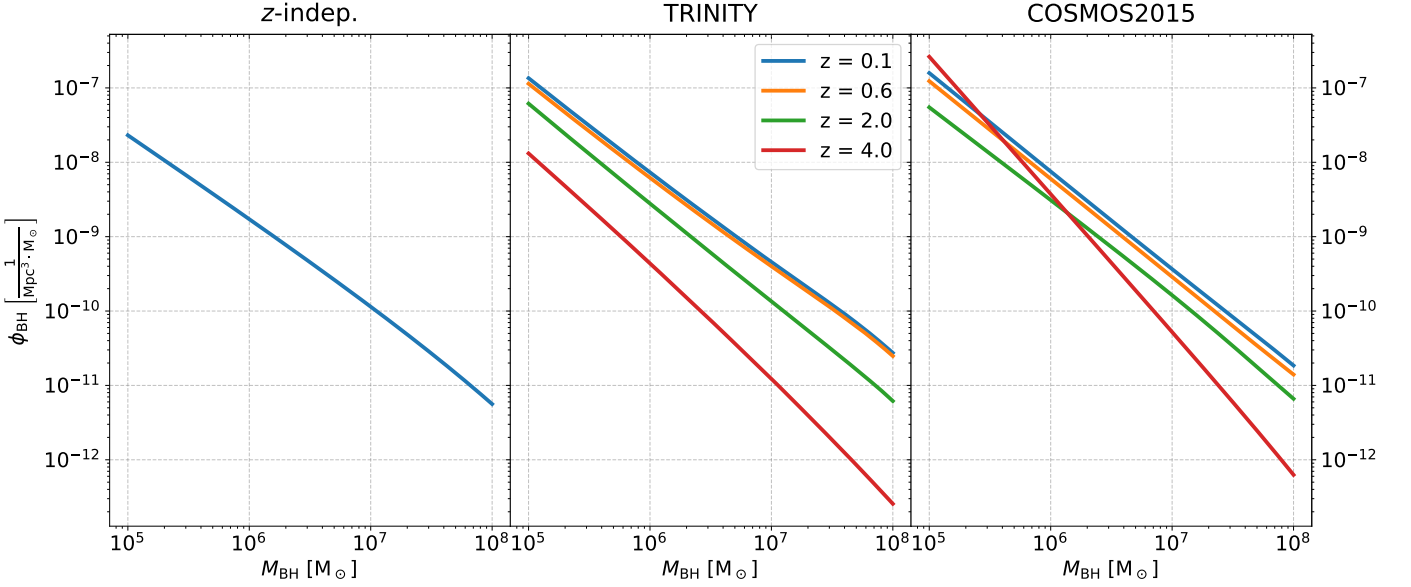


Fig. 1: The three different BHMFs we consider show significantly different redshift evolutions. Left panel: Redshift independent BHMf from Gallo & Sesana (2019). Middle panel: BHMf derived by the TRINITY model (Zhang et al. 2023). Right panel: BHMf calculated by combining a galaxy stellar mass function (GSMF) (Davidzon et al. 2017) and a BH-to-bulge mass relation (Kormendy & Ho 2013). The z -independent BHMf has a different normalization than the other two. Up to redshift 2, TRINITY and COSMOS2015 agree closely.

in terms of luminosity L and the Stefan-Boltzmann constant σ . The full solution to the integral in the numerator of the magnitude is given in Appendix A.

In the following two subsections, we present two different luminosity models for TDEs, similar to the ones considered by Szekeczes et al. (2024).

2.2.1. Phenomenological Luminosity Model

The first model is an empirical fit between the observed TDE luminosity and the debris fallback rate found by Thomsen et al. (2022):

$$L = 0.01 \cdot \dot{M}_{\text{fb}} \cdot c^2 \quad (10)$$

which assumes that the disrupted star has a stellar mass of $0.1 M_{\odot}$. Here

$$\dot{M}_{\text{fb}} = 1.49 M_{\odot} \text{ yr}^{-1} \cdot \left(\frac{f}{0.5}\right) \cdot \Xi^{\frac{3}{2}} \cdot M_{\star}^2 \cdot R_{\star}^{-\frac{3}{2}} \cdot \left(\frac{M_{\text{BH}}}{10^6 M_{\odot}}\right)^{-\frac{1}{2}} \quad (11)$$

is the mass fallback rate from Ryu et al. (2020b). It depends on the stellar mass M_{\star} , the stellar radius R_{\star} , an energy correction factor Ξ , which we explain in more detail in the next Sect. 2.2.2, and the correction factor f that accounts for different possible shapes of the energy distribution near the tails of the debris. In this first model, the debris energy spread correction factor is omitted, that is, $\Xi = 1$. The correction factor $f = 1$ for $M_{\star} \leq 0.5 M_{\odot}$ and $f = 0.5$ for $M_{\star} > 0.5 M_{\odot}$, hence, f is set to 1. Additionally, we assume a stellar radius of $0.15 R_{\odot}$. We also limit the luminosity to the Eddington limit (e.g., Rybicki & Lightman 1979)

$$L_{\text{Edd}} = 1.26 \cdot 10^{38} \text{ erg s}^{-1} \cdot \left(\frac{M_{\text{BH}}}{M_{\odot}}\right). \quad (12)$$

The first TDE luminosity model, denoted with L_1 , is then

$$L_1 = \min(L, L_{\text{Edd}}). \quad (13)$$

We show this luminosity in Fig. 2. In this model, we assume the disk's temperature to be constant. We refer to this assumption as the temperature-independent case. We perform our calculations for five temperatures $1, 2, 3, 4,$ and $5 \cdot 10^4$ K, covering the observed range of temperatures of optical TDEs (Hammerstein et al. 2023).

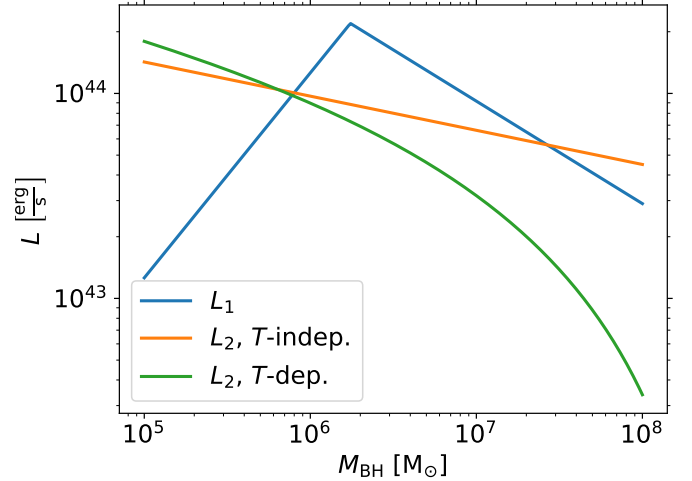


Fig. 2: Three different TDE luminosity functions dependent on BH mass. For low BH masses, L_1 is Eddington limited. The two L_2 models do not yet differ through their treatment of temperature, as temperature is not involved yet. However, they differ because of a correction factor that accounts for the spread of specific energy in the resulting debris. The T -independent model assumes this factor to be constant.

2.2.2. Theoretical Luminosity Model

The second model we consider is by Piran et al. (2015) and later improved by Ryu et al. (2020a). They propose that shocks within an eccentric accretion flow drive the light emission from a TDE. The shock is formed when earlier arriving debris, after one orbit around the BH, collides with later arriving debris. The peak luminosity

$$L_{\max} = \frac{GM_{\text{BH}}\dot{M}_{\text{fb}}}{a_0}, \quad (14)$$

depends on $a_0 = (GM_{\text{BH}})/\Delta E$, which gives the size of the mass flow. Here, G is the gravitational constant, and ΔE is the spread in specific energy. Specifically, it is the apocenter distance of most-bound debris. Combining Eqs. 11 and 14, we obtain the full expression for the second luminosity model

$$L_2 \equiv L_{\max} = \frac{\sqrt{2}G^{\frac{3}{2}}}{3\pi} \cdot M_{\star}^{\frac{8}{3}} R_{\star}^{-\frac{5}{3}} \cdot M_{\text{BH}}^{-\frac{1}{6}} \cdot \Xi^{\frac{5}{2}}. \quad (15)$$

We now split this model into two. First, following Szekerczes et al. (2024), we assume the temperature to be constant at the same values as for L_1 . Additionally, we assume all disrupted stars to be solar-like, that is, $M_{\star} = 1 M_{\odot}$ and $R_{\star} = 1 R_{\odot}$, from which follows $\Xi = 1.49$ and $f = 0.5$. We call this set of assumptions our temperature-independent L_2 model.

The second option is the case where we include the temperature dependence in this luminosity model. More specifically, we calculate the temperature in terms of BH mass. As this model includes an expression for the black body (BB) radius, it is possible to calculate an effective emission area

$$A = 2\pi \cdot a_0^2 = 2\pi \cdot \Xi_{\star}^{-2} M_{\star}^{-\frac{4}{3}} R_{\star}^2 \cdot \Xi_{\text{BH}}^{-2} M_{\text{BH}}^{\frac{4}{3}} \cdot \Xi^{-2} \quad (16)$$

of the TDE.¹ Here, we include the full energy correction factor $\Xi = \Delta\epsilon/\Delta E$ that relates the spread in specific energy ΔE to the order of magnitude estimate $\Delta\epsilon = GM_{\text{BH}}R_{\star}/r_t^2$, where $r_t = (M_{\text{BH}}/M_{\star})^{1/3}R_{\star}$ is the tidal radius. The energy correction factor $\Xi = \Xi_{\text{BH}} \cdot \Xi_{\star}$ is split into a correction from the star's internal structure

$$\Xi_{\star}(M_{\star}) = \frac{0.62 + \exp[(M_{\star} - 0.67)/0.21]}{1 + 0.55 \cdot \exp[(M_{\star} - 0.67)/0.21]} \quad (17)$$

and a correction from relativistic effects close to the BH $\Xi_{\text{BH}}(M_{\text{BH}}) = 1.27 - 0.3(M_{\text{BH}}/(10^6 M_{\odot}))^{0.242}$.

By again using the Stefan-Boltzmann law and the flux-luminosity relation, like in Eq. 9, we can solve for temperature

$$T = \left(\frac{L_2}{\sigma \cdot A}\right)^{\frac{1}{4}} = \left(\frac{\sqrt{2}G^{\frac{3}{2}}}{6\pi^2\sigma}\right)^{\frac{1}{4}} \cdot \Xi_{\star}^{\frac{9}{8}} M_{\star} R_{\star}^{-\frac{9}{8}} \cdot \Xi_{\text{BH}}^{\frac{9}{8}} M_{\text{BH}}^{-\frac{3}{8}} \quad (18)$$

instead of area. We show the dependence of the temperature of a TDE on the BH mass in Fig. 3 for a solar-like star being disrupted, that is, $M_{\star} = 1 M_{\odot}$ and $R_{\star} = 1 R_{\odot}$. The drop-off of the temperature towards the high BH mass end is due to the inclusion of the correction factor Ξ . The same influence of Ξ is also seen on the TDE luminosity in Fig. 2.

As the emitting area is known for the temperature-dependent case, the flux can directly be computed from Eq. 7. The resulting flux is compared to the fixed-temperature L_2 model in Fig. 4. For

¹ Ryu et al. (2020a) include a correction factor to account for the uncertainty in the relation between the elliptical emission area and the black body radius. However, for simplicity, we follow Ryu et al. (2020a) in assuming they are comparable.

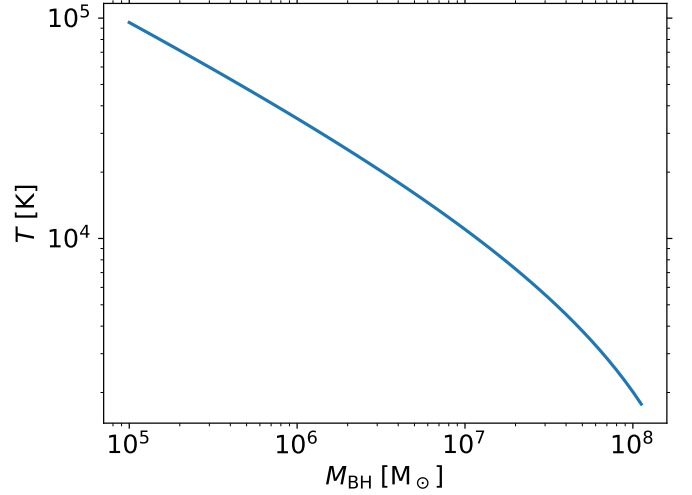


Fig. 3: TDE temperature dependent on BH mass using the L_2 model. We assume a solar-like star, that is, $M_{\star} = 1 M_{\odot}$ and $R_{\star} = 1 R_{\odot}$.

the temperature-independent models, the assumed temperature fixes the location of the BB peak and the BH mass only acts as a multiplicative factor. In the temperature-dependent case, the BH mass enters into the flux through the emission area as a factor and additionally through the temperature in the emitted specific intensity. This means the location of the BB peak is determined by the BH mass. One consequence is that the bands are sensitive to different BH mass ranges because TDEs can be observed best when the BB peak is closely aligned with the observing band.

2.3. Solving the Rate Integral

The rate integral in Eq. 1 now only depends on two parameters, the redshift and the BH mass, as we fixed the stellar mass and radius. These two parameters describe all possible TDEs we are considering. Similar to Szekerczes et al. (2024), we numerically integrate on a grid in this two-dimensional space but use a logarithmic grid spacing for the BH mass, ranging from $10^5 M_{\odot}$ to $10^8 M_{\odot}$. We choose this BH mass region because on the lower end, the existence of intermediate-mass BHs is not yet confirmed (Davis et al. 2024; Pomeroy & Norris 2024). The upper end is chosen because for $M_{\text{BH}} \gtrsim 10^8 M_{\odot}$ stars would be swallowed whole (Hills 1975) as the tidal disruption radius becomes smaller than the event horizon. To obtain the correct integral region, we calculate the observed magnitude at each grid point and only keep those that produce a magnitude brighter than the observational limit. We use the magnitude limits for ZTF and LSST as a reference. For ZTF the limits for (g, r, i) -band are (20.8, 20.6, 19.9) respectively (e.g., Bellm et al. 2019), and for LSST the limits for (u, g, r, i) are (23.3, 24.7, 24.3, 23.7), respectively (e.g., Huber et al. (2021); Lochner et al. (2022)). The assumption that a TDE is observed at peak luminosity was introduced with the mass fallback rate in Eq. 11. We relax this assumption by subtracting 0.7 from the limiting magnitude of the survey in accordance with Szekerczes et al. (2024) and Oguri & Marshall (2010). It accounts for observations not catching the TDE at its peak brightness but only close to it. The value of 0.7 gives a time window of tens of days to observe the TDE (e.g., Hinkle et al. 2020; Holoien et al. 2020). The limiting magni-

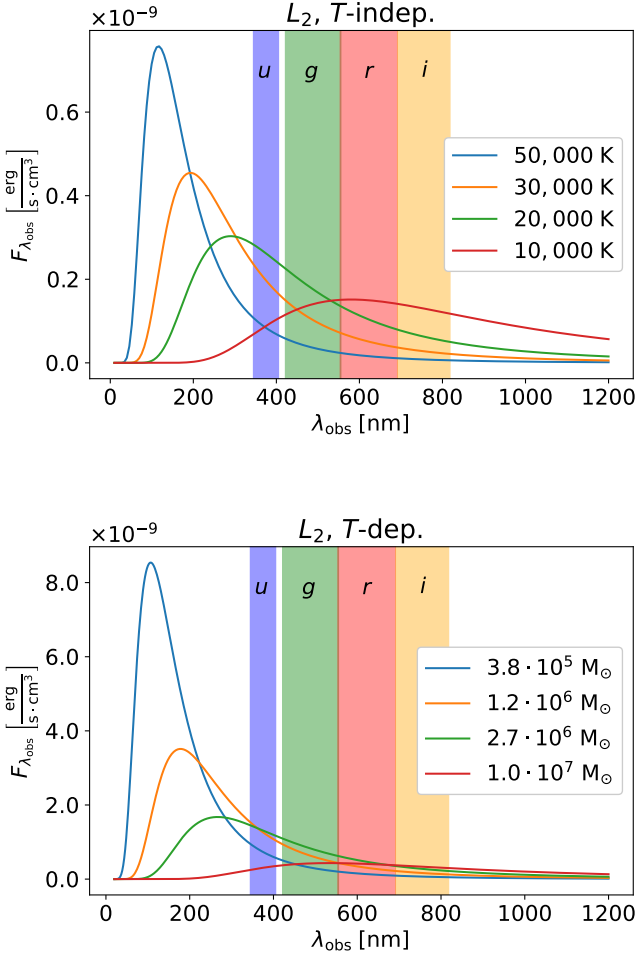


Fig. 4: Black body flux for different temperatures (upper panel) and BH masses (lower panel). For $L_2, T\text{-indep.}$ in the upper panel, $F_{\lambda_{\text{obs}}} \propto A_{\text{em}} \propto L_2 \propto M_{\text{BH}}^{-1/6}$, which means the BH mass only changes the normalization of the flux because T is fixed. For $L_2, T\text{-dep.}$ in the lower panel, $F_{\lambda_{\text{obs}}}$ has a non-trivial dependence on M_{BH} and $T \propto M_{\text{BH}}^{-3/8}$, which means the normalization and peak of the flux are coupled through the BH mass. For the top panel, we assume a BH mass of $10^6 M_{\odot}$. In the bottom panel, we choose the BH masses such that each line color matches the temperature of the fixed-temperature models. For both panels, we assume a redshift of $z = 1$.

tudes of all surveys have this subtraction incorporated from this point onward.

3. Unlensed TDE Rate

We show the results of our unlensed TDE rate calculations in Fig. 5. The vertical lines or bands represent the observational magnitude limit for ZTF and LSST. It is immediately apparent that the predictions of our considered models vary greatly. The spread easily exceeds a factor of 10^2 between the lowest and highest rates. This factor can climb above 10^3 in i and u -bands for bright limiting magnitudes ~ 19 . For faint limiting magnitudes $\gtrsim 24$, there seems to be a crossing region. Some models flatten out quicker, predicting a lower total TDE rate. It is mainly

due to a smaller BHMF at a higher redshift; fewer BHs produce fewer TDEs.

We tabulate the range of predictions for ZTF and LSST in Table 1. Independent of the TDE model, g -band observes the highest TDE rate for ZTF and LSST. In large parts, this is due to both observatories having the faintest magnitude limit in g -band.

Band	N_{TDE} for ZTF [$\text{yr}^{-1} (20,000 \text{ deg}^2)^{-1}$]	N_{TDE} for LSST [$\text{yr}^{-1} (20,000 \text{ deg}^2)^{-1}$]
u	-	920 – 34,630
g	16 – 5,440	3,580 – 82,060
r	6.5 – 5,340	1,180 – 68,320
i	1.6 – 2,350	300 – 62,380

Table 1: Predicted range of unlensed TDE rates. For ZTF, we find a scatter of $\mathcal{O}(10^3)$. For LSST, the scatter is $\mathcal{O}(10^2)$.

In the following, we individually investigate the impact of the BHMF, the luminosity model, and the temperature. We find that the assumed temperature is responsible for most of the observed scatter between the different models.

3.1. Impact of Black Hole Mass Function

First, we choose the L_2 model and fix the temperature to 20,000 K. We only exchange the BHMFs; see Fig. 6. The predicted unlensed TDE rate is highly similar for the TRINITY and the COSMOS2015 BHMFs up to a magnitude limit of 25. This is clear when comparing the two BHMFs in Fig. 1. Both are almost identical for $z \lesssim 2$, where most detectable TDEs are distributed; see Fig. B.1 for LSST limiting magnitudes. In contrast, the redshift independent model predicts lower rates by a factor of roughly 4. This is because the BHMF has a lower value at low redshift by roughly this factor of 4.

The BHMFs strongly differ at large redshifts, which we can also observe in the predicted rates. They diverge for faint magnitude limits above around 25; see Fig. 6. As the TRINITY BHMF decreases at high redshifts, the predicted TDE rates flatten out, while for the other two, only a slower increase is observed. This slowdown is attributed to the dimming of TDEs due to distance. At some point, even the brightest TDEs are too far away to reach the magnitude limit. Overall, this implies the redshift evolution of the BHMF only becomes important for faint magnitude limits above 25. These limits will not be reached by LSST, even when not considering the 0.7 reduction of the magnitude limit. However, redder bands detect the redshift evolution at a brighter magnitude than bluer bands. Red bands are naturally better suited to observe objects at high redshift. Hence, for a given magnitude limit, the highest redshift TDE always appears in i -band, allowing it to probe the redshift evolution of the BHMF at a brighter limiting magnitude than, for example, u -band. However, the temperature-dependent model can adjust for the alignment of the BB peak and the observing band. This adjustment changes the height of the BB peak by a factor of $\mathcal{O}(1)$. Hence, through the relation $m_{\text{AB}} \propto \log_{10}(F_{\lambda})$ (see Eq. 6), the magnitude only changes by an additive constant ≈ 0 . Thus, all bands detect the redshift evolution of the BHMF at the same limiting magnitude for the temperature-dependent models.

These results hint at a similar conclusion for the TDE rate per galaxy, as the BHMF and the TDE occurrence rate per galaxy influence the rate integral in the same way; see Eq. 1. A stronger redshift dependence could influence the rate integral at a brighter limiting magnitude.

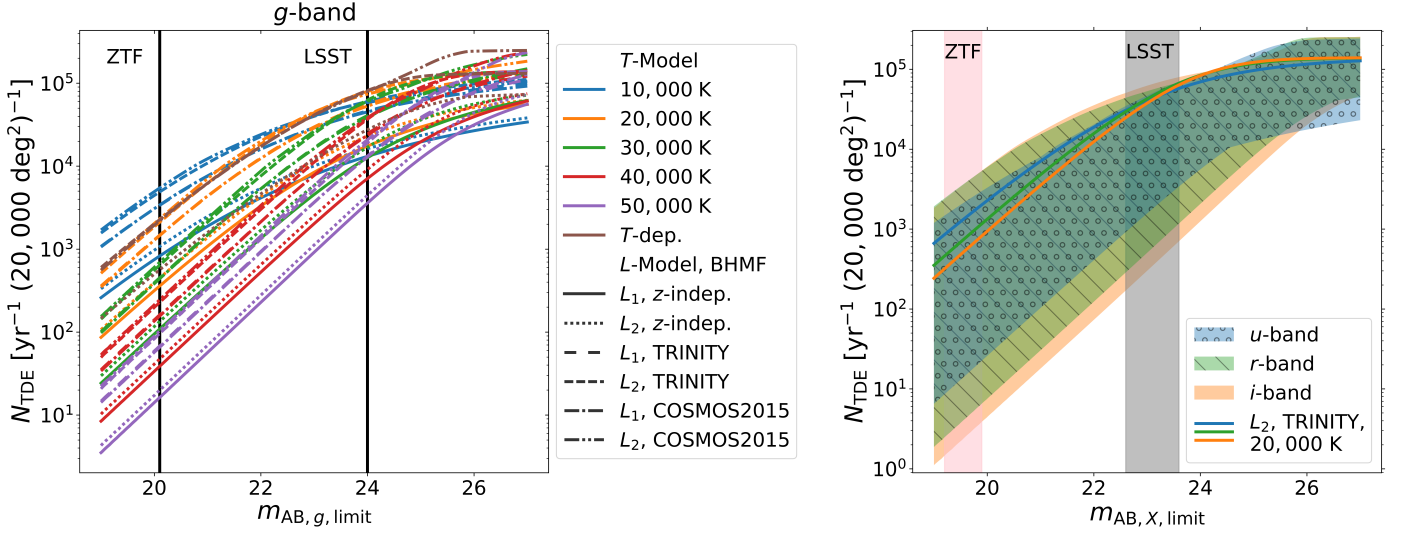


Fig. 5: Rate of TDEs as a function of survey limiting magnitude. The left panel shows the detection rate in g -band for the 33 models individually. We separate the color and line-style information to keep the legend short. The right panel shows the detection rate in u , r , and i -band, where each shaded region encompasses the spread in the models. We choose L_2 , TRINITY, 20000 K as a fiducial model to guide the eye. The 33 models we consider for the unlensed TDE rate, show a scattering factor of $\mathcal{O}(10^2)$ that can reach above $\mathcal{O}(10^3)$ for u and i -band. The vertical black lines (left panel) or the colorful strips (right panel) show the observational magnitude limit for ZTF (g , r , i -band) and LSST (u , g , r , i -band).

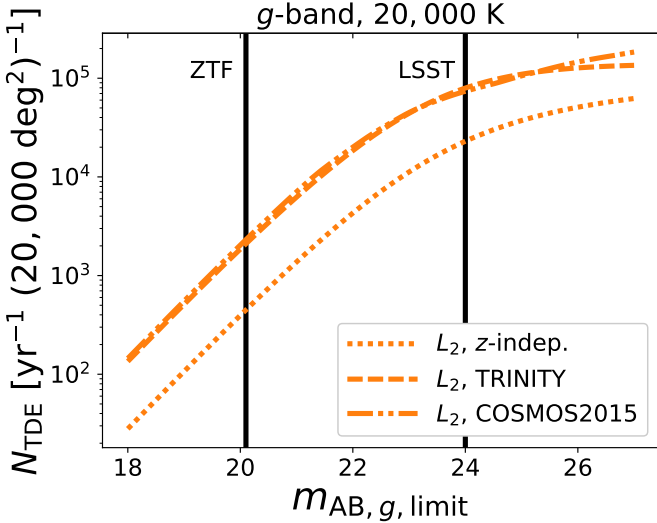


Fig. 6: Rate of TDEs as a function of survey limiting magnitude. Only the local BHMF impacts the unlensed TDE rates observed by current and near-future surveys such as ZTF and LSST. The redshift evolution of the BHMF influences the rate from a limiting magnitude of 25 onward. We have taken a representative subset from the left panel of Fig. 5 to clearly show the influence of the BHMF.

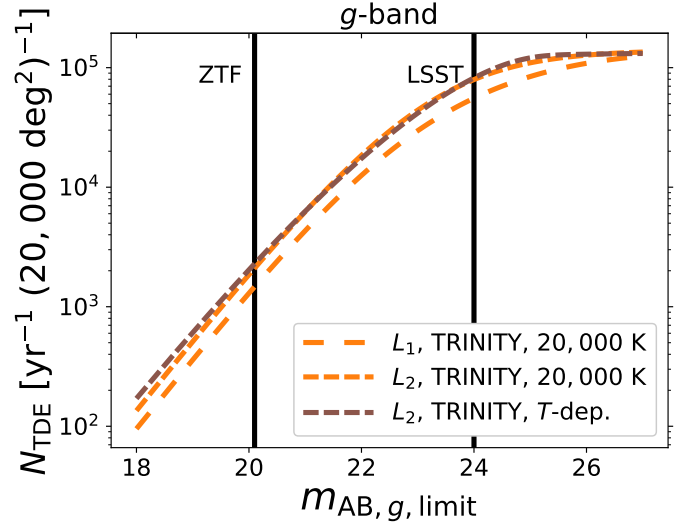


Fig. 7: Rate of TDEs as a function of survey limiting magnitude for different luminosity models. The luminosity model has little impact on the unlensed TDE rate. It can introduce a dependence of the rate on the observing band for the fixed-temperature models. The temperature-dependent model can compensate for the chosen observing band by selecting the TDE temperature. Thus, it does not show a strong band dependence. We have taken a representative subset from the left panel of Fig. 5 to clearly show the influence of the luminosity model.

3.2. Impact of Luminosity Model

Here, we fix the TRINITY BHMF and let the luminosity function vary; see Fig. 7. The two fixed-temperature luminosity models don't differ strongly in their unlensed TDE rate predictions. L_2 produces higher rates across almost all limiting magnitudes in all bands than L_1 . No matter the BHMF, the integrand of the rate integral (see Eq. 1) has a small but negative dependence on

BH mass. Therefore, TDEs with a lower BH mass are preferred, which are brighter for L_2 compared to L_1 .

This trend holds until around a magnitude limit of 27, where both rates meet. L_2 flattens out quicker than L_1 . This is due to the higher maximal luminosity that L_1 allows for; see Fig. 2. At a given magnitude limit, this fact implies that TDEs can be

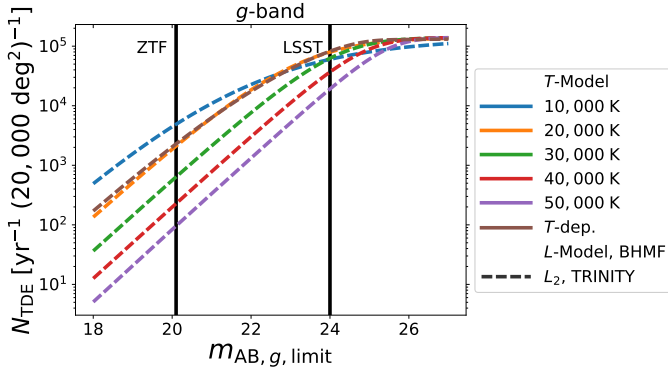


Fig. 8: Rate of TDEs as a function of survey limiting magnitude. The chosen temperature has the largest impact on the unlensed TDE rate. This parameter accounts for most of the scatter observed between the different models. This implies that it is crucial that the BB peak and the observing band are well aligned. We have taken a representative subset from the left panel of Fig. 5 to clearly show the influence of the temperature.

observed at larger redshift for L_1 , meaning the volume in which observable TDEs can take place is larger.

For the temperature-dependent model, the peak luminosity is higher than that for the fixed temperature L_2 model. But TDEs with high BH masses are suppressed with a lower luminosity. These two effects cancel, such that almost the same rate of TDEs is observed for the temperature-dependent and the temperature-independent case.

3.3. Impact of Temperature

The assumed temperature contributes the most to the spread of the models; see Fig. 8. The temperature strongly impacts the redshift distribution of the observed TDEs. As explained above, it is crucial that the peak of the BB spectrum aligns well with the observing band. At low redshift, the closest alignment is seen for 10,000 K; hence, models with this temperature show the highest rates at bright limiting magnitudes $\lesssim 22$. The BB peak is always shifted into a given observing band at some redshift. Therefore, when a faint limiting magnitude $\gtrsim 26$ is assumed, all bands should roughly observe the same number of TDEs as every TDE can be observed in every band. This is what we observe in Fig. 8. The odd one out is the 10,000 K model, not quite reaching the same level as the other temperatures. The same deviation is more prominent in u -band but not seen in r or i -band. For this temperature, the peak of the BB spectrum lies at 290 nm at $z = 0$, just at a smaller wavelength than u -band. But the integrand in the numerator of the magnitude is proportional to $\lambda \cdot F_{\lambda_{\text{obs}}}$ (see Eq. 6), meaning longer wavelengths are weighted more. With increasing redshift, the steep rise of the BB spectrum with increasing wavelength quickly dims the TDEs as the peak of the BB shifts out of the u -band and even g -band to longer wavelengths. For higher temperatures, the peak of the BB spectrum is first shifted into the observing band, counteracting the dimming due to distance. Therefore, TDEs are only observed at fainter magnitudes for 10,000 K, contributing to this model's shallower slope. Hence, it takes longer to catch up to the models.

3.4. Comparison to the Observed Rate

Hammerstein et al. (2023) report that ZTF observed 30 TDEs in 2.6 years in multi-band observations using g and r -bands. ZTF observed the entire visible northern sky, roughly speaking around $20,000 \text{ deg}^2$. This means they find an unlensed TDE rate N_{TDE} of around $10 \text{ to } 15 \text{ yr}^{-1} (20,000 \text{ deg}^2)^{-1}$. In g -band, this rate is below all our models. The lowest prediction is $16.5 \text{ yr}^{-1} (20,000 \text{ deg}^2)^{-1}$ from the L_1 , z -independent, 50,000 K model. For r -band, the rate lies between the L_1 , 40,000 K and L_2 , 50,000 K models, both for the redshift-independent BHMF.

Hammerstein et al. (2023) also infer the temperature and find a range of around 15,000 K to 35,000 K with an average of 20,783 K. For this temperature range, our models would predict $108 (L_1, z\text{-indep.}, 30,000 \text{ K})$ to $2,313 \text{ yr}^{-1} (20,000 \text{ deg}^2)^{-1}$ (L_2 , COSMOS2015, 20,000 K) in g -band and $49.5 (L_1, z\text{-indep.}, 30,000 \text{ K})$ to $1,538 \text{ yr}^{-1} (20,000 \text{ deg}^2)^{-1}$ (L_2 , TRINITY, T -dep.) in r -band. In our calculation, we have not accounted for the effective year length of ZTF, which might lead to more incomplete observations than our models predict. We have also not accounted for other observational constraints, such as dust extinction or the host galaxy's light. The implicit assumption is that a TDE is always observable. In practice, some TDEs go undetected because of the bright host galaxy. In addition, we have also not accounted for the completeness. The identification of TDEs is an active field of research (e.g., Zabludoff et al. 2021; Gomez et al. 2023; Stein et al. 2024). On top of that, removing the assumptions that every star is solar-like and every TDE is a full disruption could notably enhance the results. Whether these effects can account for a factor of 10^2 or can only explain part of the overestimation needs further analysis.

The inferred BH mass does also yield little insight. Hammerstein et al. (2023) infer a range between $10^6 M_{\odot}$ and $10^7 M_{\odot}$ using TDEmass (Ryu et al. 2020a) and a range from $2 \cdot 10^6 M_{\odot}$ to $4 \cdot 10^7 M_{\odot}$ using MOSFiT (Guillochon et al. 2018; Mockler et al. 2019). These peak around the same mass as the L_1 and the temperature-dependent L_2 models, respectively. But as the BH mass is observationally not well constrained, we cannot establish a TDE luminosity model here. Nevertheless, this may indicate the possibility of inferring the TDE luminosity model using the BH mass distribution. This is especially feasible when better statistics become available with the launch of LSST. However, the BH mass must be measured robustly for such an investigation.

4. Lensed TDE Rate

4.1. Calculating the Lensed Rates

The lensed TDE rate is calculated with the code developed by Oguri & Marshall (2010). Some optimizations have been introduced to the code to speed up calculation times significantly. For details, refer to Appendix C. For the calculations, the code from Oguri & Marshall (2010) assumes that all lens galaxies are singular isothermal ellipsoids with convergence

$$\kappa = \frac{\theta_E}{2} \cdot \frac{\lambda(e)}{\sqrt{(1-e)^{-1} \cdot x^2 + (1-e) \cdot y^2}}, \quad (19)$$

where $\lambda(e)$ is the dynamical normalization, e is the ellipticity, and

$$\theta_E = 4\pi \cdot \left(\frac{v}{c}\right)^2 \cdot \frac{D_{\text{ds}}}{D_s} \quad (20)$$

the Einstein radius, dependent on the velocity dispersion v of the lens galaxy, the angular diameter distance from the observer to the source D_s , and from the lens to the source D_{ls} . These equations for the singular isothermal ellipsoid were derived by Kormann et al. (1994). The code calculates a lensed TDE mock catalog by taking in an unlensed mock catalog and simulating all possible lens galaxies as elliptical galaxies, which make up $\sim 80\%$ of the lensing probability (Turner et al. 1984; Fukugita et al. 1992; Kochanek 1996; Chae 2003; Oguri 2006; Möller et al. 2007). Hence, every lens can be described by its redshift and velocity dispersion in a two-dimensional parameter space. The same technique for generating a mock catalog of unlensed TDEs can now be used to create a catalog of possible lens galaxies. By estimating an area on the sky larger than any possible lens system, they can calculate a rate of finding a TDE in the vicinity of a lens galaxy, assuming both are spread uniformly on the survey area. This assumption is equivalent to the isotropy of the universe (e.g., Goodman 1995; Clarkson & Maartens 2010; Kumar Aluri et al. 2023; Bengaly et al. 2024). By sampling a Poisson distribution with that rate estimate, they can find the number of candidate systems. The lens equation is then solved for these systems to determine whether it is an actual lens or just a close separation with no multiple images. All systems that produce multiple images are then saved to a mock catalog. A TDE lensed into a double is considered observable when both images are brighter than the limiting magnitude. The third brightest image must be brighter than the magnitude limit for a quad lensed TDE. Calculating rates from such a mock catalog is as simple as counting the entries brighter than the magnitude limit. But, to calculate rates smaller than $1 \text{ yr}^{-1} (20,000 \text{ deg}^2)^{-1}$, we need to oversample. We achieve this by calculating N catalogs and, in the end, dividing the summed number of systems by N . Thus, every entry in a mock catalog only counts as $1/N$ towards the rate. This mock catalog counting suffers from Poisson noise, so the error scales with $1/\sqrt{N}$.

4.2. Lensed Rate Results

Following Szekerczes et al. (2024), we only select lensed events with an image separation in the range $[0.5'', 4'']$ to ensure that the multiple images can be resolved by ground-based surveys such as LSST. For a quad, we measure the maximal distance between two images. Here, we include all images of a quad. In a cusp configuration, the fourth image typically sets the largest image separation, but it is also demagnified. However, deeper imaging can reveal it, and we consider the system resolvable. We only consider the lensed rate for LSST limiting magnitudes. We don't examine ZTF limits here because many models predict a smaller rate than our numerical limit of $10^{-3} \text{ yr}^{-1} (20,000 \text{ deg}^2)^{-1}$, with an oversampling factor of 1000.

The lensed rates show, just like the unlensed ones, a large scatter of $O(10^2)$ in the four bands; see Fig. 9. The overall trend is similar to the unlensed rates. Initially, the rate increases steeply and flattens towards fainter limiting magnitudes around 25 or 26. For LSST, we tabulate the range of predictions in Table 2. Just as for the unlensed rates, only the local BHMF is important for the rate prediction. The redshift evolution of the BHMF only impacts the rate for magnitude limits fainter than those reached by LSST. The lensed rate shows the influence of the redshift evolution at a brighter limiting magnitude of 24 than the unlensed rate because the magnification due to lensing allows us to observe TDEs at a greater distance from us. The main contribution to the scattering of the different models still stems

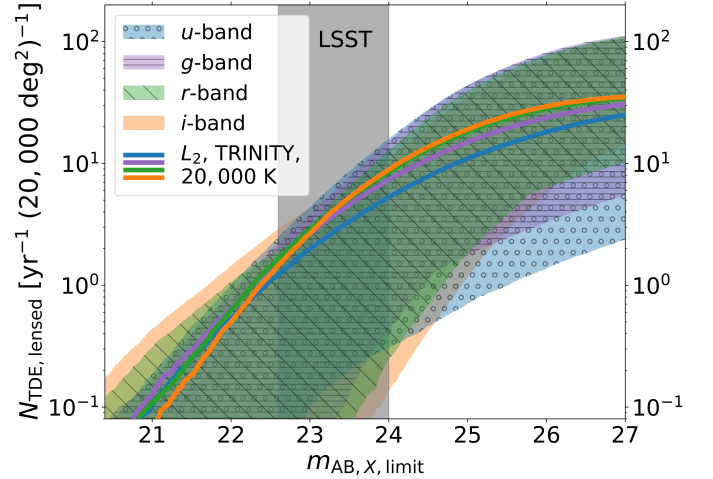


Fig. 9: Rates of lensed TDEs as a function of survey limiting magnitude. The lensed TDE rates also show a scattering factor of $O(10^2)$ that can almost reach $O(10^3)$. The gray strip shows the observational magnitude limit for LSST (u, g, r, i -band). We display L_2 , TRINITY, 20,000 K as a fiducial model in solid lines to guide the eye.

from the assumed temperature. The luminosity model has, just as in the unlensed case, little impact on the lensed TDE rate.

Band	$N_{\text{TDE,lensed}}$ for LSST [$\text{yr}^{-1} (20,000 \text{ deg}^2)^{-1}$]
u	0.04 – 2.49
g	0.43 – 15
r	0.09 – 7.4
i	0.008 – 4.3

Table 2: Predicted range of lensed TDE rates. For LSST, we observe a scatter of $O(10^2)$ in each band.

4.3. Lensed Fraction

The unlensed and lensed TDE rate predictions both exhibit a broad spread. Therefore, we further investigate the lensed fraction to estimate the fraction of observed TDEs that are part of a lensing system. We present in Fig. 10 the lensed fractions for LSST magnitude limits. In the plot, each point or line indicates the ratio of observable lensed TDEs to observable unlensed TDEs given a LSST magnitude limit. The horizontal lines are used for the temperature-dependent L_2 models, which cover a wide range of possible TDE temperatures. The lensed fraction is more robust against the different model parameters and displays a smaller scattering factor of ~ 50 between the lowest and highest fractions. We predict the fraction of lensed to unlensed TDEs to be between $1.7 \cdot 10^{-5}$ (L_1 , TRINITY, 10,000 K, u -band) and $8.7 \cdot 10^{-4}$ (L_1 , z -indep., 50,000 K, g -band). As an order of magnitude, we can say that in order to observe one lensed TDE, LSST has to observe thousands to tens of thousands of unlensed TDEs.

The lensed TDE population includes many TDEs at a higher redshift than found in the unlensed population. Thus, a larger lensed fraction implies that the fading of TDEs is more strongly counteracted either due to an increasing BHMF with redshift or due to a better BB peak alignment. Overall, we can interpret

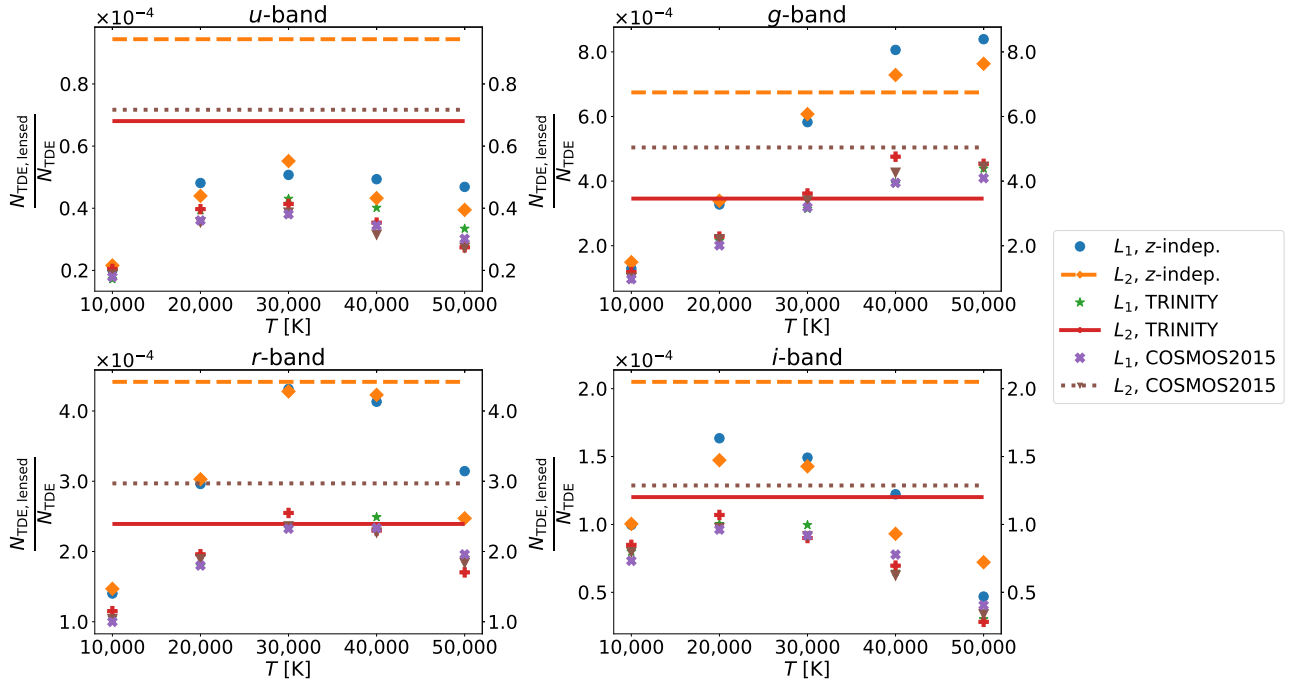


Fig. 10: Lensed fraction for the different TDE models. Each point represents the fraction of TDEs observed as part of a lensing system. The lines are used for the temperature-dependent L_2 models. The fractions of lensed TDEs show a greatly reduced scatter than the scatter of the unlensed and lensed rates. The fractions lie within a factor of 50. We calculate these lensed fractions for LSST magnitude limits.

the lensed fraction as a value that compares the number of observable TDEs at low and high redshifts. This becomes further clear when comparing the first row of Fig. 11 to the first row of Fig. B.1. The lensed TDEs have a median redshift between 2 and 3, while the unlensed TDEs have a median redshift between 0.2 and 0.7.

To better understand Fig. 10, we consider the observing bands individually. In u -band, we observe the smallest lensed fractions. Here, we know that a temperature of 10,000 K aligns the BB peak well with u -band at low redshifts. But this alignment is broken at larger redshifts, and only a few TDEs are observed. Thus, we find a small lensed fraction. The fraction increases with temperature because the low redshift alignment of the BB peak gets worse, while the alignment gets better for a larger redshift. We expect most lensed TDEs to be around $z = 1$; see the first row of Fig. 11. At this redshift, a temperature between 20,000 K and 30,000 K is best aligned with u -band. Hence, we do not expect the increasing trend of the lensed fraction to continue much beyond this temperature. The temperature-dependent models can compensate for BB peak alignment and reach higher temperatures and redshifts. Therefore, they observe many TDEs at low redshift. But with the possibility of very high temperatures, they produce many observable TDEs in u -band at high redshift. Thus, temperature-dependent models yield the highest fraction in u -band.

The same trend of the lensed fraction is seen in g -band; see the upper right panel of Fig. 10. But the rising of the fraction continues up to 50,000 K. This is due to the possibility of observing lensed TDEs up to $z \lesssim 4$ in g -band, while unlensed ones fade from view at $z \gtrsim 0.7$.

In r and i -band, the peak of the lensed fraction moves to lower temperatures because these temperatures perform best in the respective bands at high redshifts. It is worth noting that in i -band at 50,000 K, we find the lowest lensed fraction, despite the

fact that i -band observes very few unlensed TDEs at this temperature. But i -band lies too far away from the BB peak. Hence, the dimming due to distance fades any lensed TDE from view long before the BB peak can be aligned with the band. Therefore, i -band is not observing many lensed TDEs either, indicating a small lensed fraction.

The different BHMFS seem to amplify the influence of the temperature. Comparing the two redshift-dependent BHMFS, we can see that the COSMOS2015 BHMFS increases the fraction compared to the TRINITY BHMFS only for the temperature-dependent model. This is because the temperature-dependent model reaches the highest redshift; see the first row of Fig. 11. Therefore, the redshift evolution can no longer be neglected, and the increase of the COSMOS2015 BHMFS for low mass BHs does matter. The redshift-independent BHMFS amplifies the influence of the temperature the most. This makes sense as a decreasing BHMFS with redshift always leads to a decrease in TDEs observed at high redshift. The redshift-independent one does not show any evolution and, therefore, can more easily produce high TDE rates at high redshift.

4.4. Lensing Parameters

Lastly, we investigate different parameters of the lensed TDE population. We select a subset of 5 models to allow each parameter or combination of parameters to be varied. The distributions shown are for LSST limiting magnitudes in Fig. 11.

First, we consider the TDE parameters: source redshift and BH mass; see the first and second rows of Fig. 11, respectively. We expect most lensed TDEs to be observed between redshift 1 and 2. Overall, g -band is always best suited to observe TDEs because it has the faintest limiting magnitude. As expected, the BH mass distribution follows the shape of the magnitude functions.

The brighter TDEs at a given BH mass, the more of these TDEs are observed.

Second, we assess the lens parameters, which are the lens redshift and lens velocity dispersion; see the third and fourth rows of Fig. 11, respectively. As expected, the TDE model has little to no effect on the lenses. For the temperature-dependent and the 40,000 K models, we do observe lenses at a higher redshift, but this is solely due to the fact that in these models, TDEs can also be observed at a larger redshift. Most lenses sit at $z \lesssim 1$ and have a velocity dispersion between 100 and 300 km s⁻¹.

Third, we examine the parameters of the resulting lens system. The image separation in the fifth row and the time delay of doubles in the sixth row of Fig. 11, as well as the ratio of double to quad lenses in Table 3. For quads, the maximal image separation is taken. These parameters are also largely independent of the chosen TDE model. Only the fact that some models predict TDEs at higher redshifts influences the distributions. Most images have an image separation below 3'', but the smaller the image separation, the more probable such a system is. As mentioned earlier, the image separation was cut at 0.5''. Similarly independent is the time delay of doubles. Most lens systems display a time delay ranging from a few days to around 100 days. Models that predict TDEs at higher redshifts also observe longer time delays. Quads show a very similar time-delay distribution for the longest time delay. The second and third time-delay distributions are shifted to shorter time delays. Their peak is around 4 days instead of around 11 days. Their distributions are shown in Appendix D.

Our analysis suggests around three or four doubles for one quad system. In Table 3, the ratio of doubles to quads falls into a range from 0.96 to 5.41. Here, the maximal redshift of the different TDE models plays a large role in the ratio of doubles to quads. Doubles typically prefer lower redshifts, while quads prefer higher redshifts. The exemplary L_2 , COSMOS2015, 20 000 K model clearly shows that the quad lenses peak around redshift 2, while the double lenses peak approximately at $z = 1$ in g , r and i -bands. For u -band, quads also peak at a higher redshift than doubles. This difference in the preferred redshift is due to the fact that the tangential caustic typically provides a higher magnification than the radial caustic (Venumadhav et al. 2017; Meena et al. 2022). Therefore, quads are more likely to receive a large boost in brightness and are more likely to be observed at great distances. If a given TDE model predicts more lensed TDEs at low redshifts compared to another model, we expect the former one to display a larger ratio. In Table 3, we also calculate the fraction of quad lenses relative to the total number of lensed TDEs. We find that between 16 to 39% of lensed TDEs will be a quad system. Oguri & Marshall (2010) predict in their catalogs for LSST that 13% of lensed quasars and 30 to 32% of lensed supernovae will be observed as quad lenses. Hence, our results are comparable to their findings.

5. Conclusion

In this paper, we have numerically calculated the predicted unlensed and lensed TDE rate as a function of limiting magnitude in four bands. We covered the ongoing ZTF and the future LSST surveys and different model parameters such as the BHMF, TDE luminosity model, and assumed flare temperature. For the unlensed rates, our models predict between 16 and 5,440 yr⁻¹ (20,000 deg²)⁻¹ for ZTF in g -band. For LSST, the rate is in the range from 3,580 to 82,060 yr⁻¹ (20,000 deg²)⁻¹. In both surveys, g -band stands out as the best option to ob-

Model	Band	Doubles	Quads	$\frac{N_{\text{doubles}}}{N_{\text{quads}}}$	$\frac{N_{\text{quads}}}{N_{\text{TDE,lensed}}}$
		Rate	Rate		[%]
L_1 , TRINITY, 20 000 K	u	0.63	0.2	3.18	23.91
	g	3.86	0.77	5.03	16.58
	r	2.82	0.69	4.12	19.54
	i	1.26	0.41	3.07	24.58
L_2 , TRINITY, 20 000 K	u	0.97	0.26	3.78	20.92
	g	6.15	1.14	5.41	15.6
	r	4.61	1.15	4.02	19.92
	i	1.98	0.67	2.94	25.4
L_2 , TRINITY T -dep.	u	1.7	0.6	2.81	26.22
	g	8.63	1.8	4.81	17.22
	r	4.98	1.28	3.89	20.43
	i	2.06	0.67	3.09	24.46
L_2 , TRINITY, 40 000 K	u	0.22	0.14	1.56	39.13
	g	2.26	0.85	2.65	27.41
	r	0.56	0.35	1.58	38.71
	i	0.08	0.09	0.96	50.9
L_2 , COSMOS2015, 20 000 K	u	0.9	0.24	3.75	21.04
	g	5.92	1.38	4.29	18.91
	r	4.42	1.37	3.24	23.59
	i	1.78	0.78	2.28	30.5

Table 3: The rate of double and quad lensed TDEs in per year and 20 000 deg², as well as the ratio of double to quad lenses and the fraction of quad to total lenses. We expect to find a few doubles for every quad. This table is calculated for LSST magnitude limits.

serve TDEs because it has the faintest limiting magnitude. The sizable scattering factor of $O(10^2)$ up to $\sim 10^3$ that the models display can be attributed to the assumed TDE temperature, making it the most critical assumption for TDE rate estimates. Despite the uncertain predictions, we demonstrate that only the local BHMF is relevant for current and near-future surveys. Our redshift-dependent BHMF only showed a significant deviation from the redshift-independent model at a limiting magnitude of 25 or fainter. As LSST will only reach about magnitude 24, the redshift evolution of the BHMF is not important to LSST. Compared to the observational unlensed TDE rate around 10 to 15 yr⁻¹ (20,000 deg²)⁻¹ obtained from ZTF, most of our models overestimate the rate. It should be expected that we overestimate the observed rate, as we have not accounted for completeness or any observational effects in our calculations. For a more accurate estimate in the future, we could include the host galaxy light or dust extinction to better match observations. Furthermore, removing the assumption that every star is solar-like would yield even more accurate results. Last, certain physical processes in TDEs can also make the detected TDE rates significantly deviate from the theoretical rates (Wong et al. 2022).

From our investigation into the lensed fraction, we can approximate that for every 10,000 unlensed TDEs, we expect LSST to find a few lensed events. The results show a reduced scatter to around a factor of 50. As our unlensed rates only poorly match observational ones, it seems improbable that a large sample of hundreds of lensed TDEs can be obtained. Yet, LSST will observe a few lensed TDEs over its 10-year survey time. Lensed TDEs are also best observed in g -band due to its faint limiting magnitude. For LSST, our predictions range from one every two years to more than ten yearly, assuming 20,000 deg² in g -band, still showing much of the scatter also observed for the unlensed rate. However, analogously to the unlensed rate, we were able to show that the TDE temperature is the most important assumption and only the BHMF is relevant even beyond LSST limiting magnitudes.

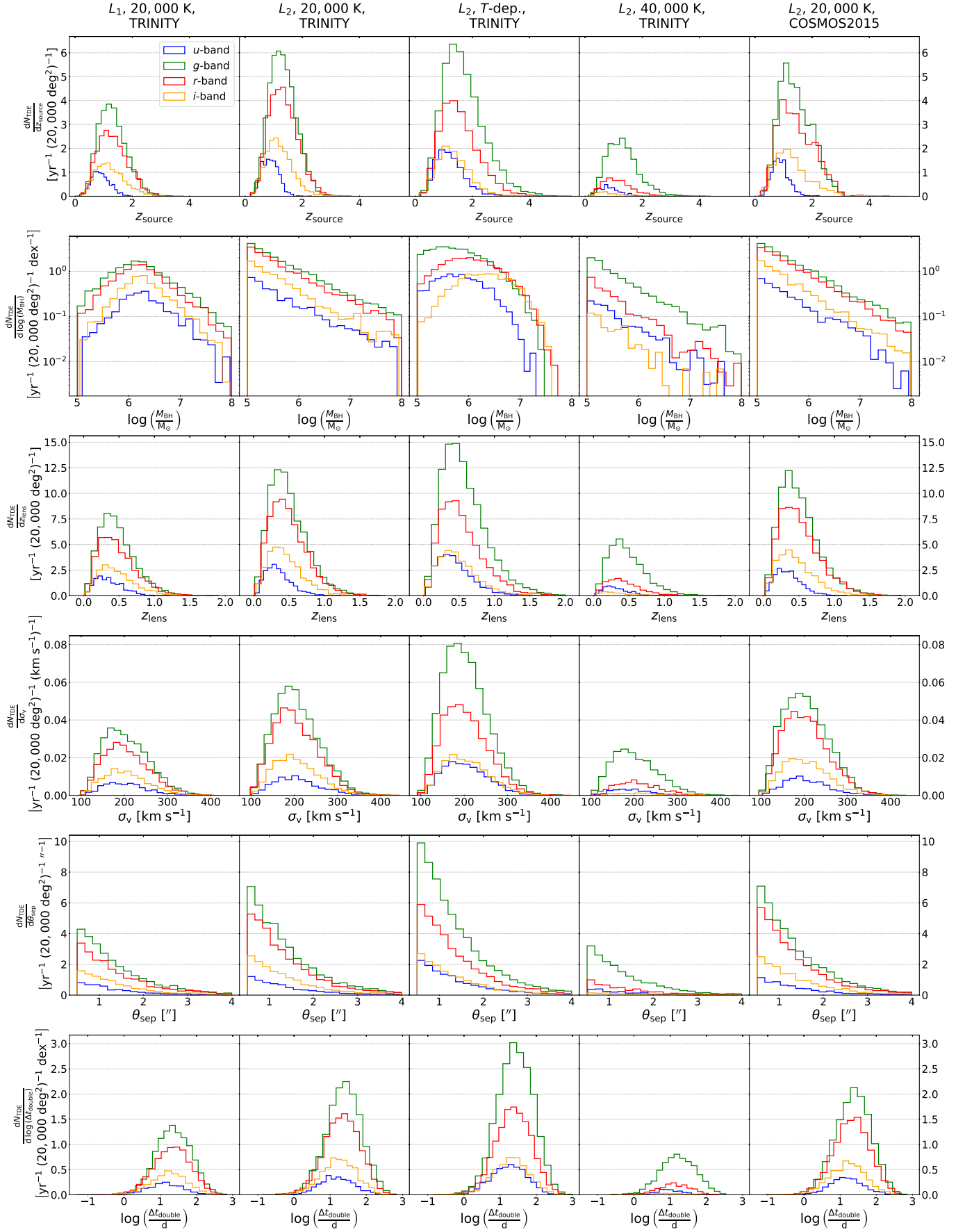


Fig. 11: Differential rate of lensed TDEs for five representative models. The rows from top to bottom are the TDE redshifts, BH masses, lens redshifts, lens velocity dispersions, lensed image separations, and doubles' time delays. The three time delays for quads are shown in Appendix D. These figures are calculated for LSST magnitude limits.

Acknowledgements. We thank Volker Springel for the helpful discussion on BHMFs. EM and SHS thank the Max Planck Society for support through the Max Planck Fellowship for SHS. KS acknowledges support through a Fulbright grant of the German-American Fulbright Commission. LD acknowledges the support from the Hong Kong Research Grants Council (17304821, 17314822, 17305124). This work was supported by JSPS KAKENHI Grant Numbers JP23K22531, JP22K21349, JP19KK0076.

References

- Baehr, H. D. & Kabelac, S. 2016, *Thermodynamik* (Springer)
- Bellm, E. C., Kulkarni, S. R., Graham, M. J., et al. 2019, *PASP*, 131, 018002
- Bengaly, C. A. P., Alcaniz, J. S., & Pigozzo, C. 2024, *Phys. Rev. D*, 109, 123553
- Bessell, M. & Murphy, S. 2012, *PASP*, 124, 140
- Bricman, K. & Gomboc, A. 2020, *ApJ*, 890, 73
- Chae, K.-H. 2003, *MNRAS*, 346, 746
- Clarkson, C. & Maartens, R. 2010, *Classical and Quantum Gravity*, 27, 124008
- Davidzon, I., Ilbert, O., Laigle, C., et al. 2017, *A&A*, 605, A70
- Davis, B. L., Graham, A. W., Soria, R., et al. 2024, *ApJ*, 971, 123
- Fukugita, M., Futamase, T., Kasai, M., & Turner, E. L. 1992, *ApJ*, 393, 3
- Gallo, E. & Sesana, A. 2019, *ApJ*, 883, L18
- Gezari, S. 2013, in *American Astronomical Society Meeting Abstracts*, Vol. 221, American Astronomical Society Meeting Abstracts #221, 131.02
- Gezari, S. 2021, *ARA&A*, 59, 21
- Gomez, S., Villar, V. A., Berger, E., et al. 2023, *ApJ*, 949, 113
- Goodman, J. 1995, *Phys. Rev. D*, 52, 1821
- Guillochon, J., Nicholl, M., Villar, V. A., et al. 2018, *ApJS*, 236, 6
- Hammerstein, E., van Velzen, S., Gezari, S., et al. 2023, *ApJ*, 942, 9
- Hills, J. G. 1975, *Nature*, 254, 295
- Hills, J. G. 1988, *Nature*, 331, 687
- Hinkle, J. T., Holoien, T. W. S., Shappee, B. J., et al. 2020, *ApJ*, 894, L10
- Holoien, T. W. S., Auchettl, K., Tucker, M. A., et al. 2020, *ApJ*, 898, 161
- Huber, S., Suyu, S., Noebauer, U. M., et al. 2021, *A&A*, 646, A110
- Ivezic, Z., Kahn, S. M., Tyson, J. A., et al. 2019, *ApJ*, 873, 111
- Kochanek, C. S. 1996, *ApJ*, 466, 638
- Kochanek, C. S. 2004, *ApJ*, 605, 58
- Kormann, R., Schneider, P., & Bartelmann, M. 1994, *A&A*, 284, 285
- Kormendy, J. & Ho, L. C. 2013, *ARA&A*, 51, 511
- Kumar Aluri, P., Cea, P., Chingambam, P., et al. 2023, *Classical and Quantum Gravity*, 40, 094001
- Laigle, C., McCracken, H. J., Ilbert, O., et al. 2016, *ApJS*, 224, 24
- Lin, D., Guillochon, J., Komossa, S., et al. 2017, *New A*, 1, 0033
- Lin, Z., Jiang, N., & Kong, X. 2022, *MNRAS*, 513, 2422
- Lochner, M., Scolnic, D., Almoubayyed, H., et al. 2022, *ApJS*, 259, 58
- Meena, A. K., Arad, O., & Zitrin, A. 2022, *MNRAS*, 514, 2545
- Mockler, B., Guillochon, J., & Ramirez-Ruiz, E. 2019, *ApJ*, 872, 151
- Möller, O., Kitzbichler, M., & Natarajan, P. 2007, *MNRAS*, 379, 1195
- Oguri, M. 2006, *MNRAS*, 367, 1241
- Oguri, M. & Marshall, P. J. 2010, *MNRAS*, 405, 2579
- Pfister, H., Volonteri, M., Dai, L., & Colpi, M. 2020, *MNRAS*, 497, 2276
- Piran, T., Svirski, G., Krolik, J., Cheng, R. M., & Shiokawa, H. 2015, *ApJ*, 806, 164
- Planck, M. 1901, *Annalen der Physik*, 309, 553
- Pomeroy, R. T. & Norris, M. A. 2024, *MNRAS*, 530, 3043
- Rees, M. J. 1988, *Nature*, 333, 523
- Refsdal, S. 1964, *MNRAS*, 128, 307
- Rybicki, G. B. & Lightman, A. P. 1979, *Radiative processes in astrophysics* (John Wiley & Sons)
- Ryu, T., Krolik, J., & Piran, T. 2020a, *ApJ*, 904, 73
- Ryu, T., Krolik, J., Piran, T., & Noble, S. C. 2020b, *ApJ*, 904, 98
- Shimizu, T., Oogi, T., Okamoto, T., Nagashima, M., & Enoki, M. 2024, *MNRAS*, 531, 851
- Stein, R., Mahabal, A., Reusch, S., et al. 2024, *ApJ*, 965, L14
- Szekerces, K., Ryu, T., Suyu, S. H., et al. 2024, *A&A*, 690, A384
- Thomsen, L. L., Kwan, T. M., Dai, L., et al. 2022, *ApJ*, 937, L28
- Turner, E. L., Ostriker, J. P., & Gott, III, J. R. 1984, *ApJ*, 284, 1
- Venumadhav, T., Dai, L., & Miralda-Escudé, J. 2017, *ApJ*, 850, 49
- Wong, T. H. T., Pfister, H., & Dai, L. 2022, *ApJ*, 927, L19
- Wozniak, P. R., Graham, M. J., Mahabal, A. A., & Seaman, R., eds. 2014, *The Third Hot-wiring the Transient Universe Workshop (HTU-III)*
- Zabludoff, A., Arcavi, I., LaMassa, S., et al. 2021, *Space Sci. Rev.*, 217, 54
- Zhang, H., Behroozi, P., Volonteri, M., et al. 2023, *MNRAS*, 518, 2123

Appendix A: Magnitude Integral

To calculate the flux integral in the numerator of Eq. 6, we will first introduce the variables a and b to simplify calculations. The flux now takes the form

$$F_{\lambda_{\text{obs}},0} = \frac{a}{\lambda_{\text{obs}}^5} \cdot \frac{1}{e^{\frac{b}{\lambda_{\text{obs}}}} - 1}.$$

Compare to Eq. 7 for the expressions of a and b . The integral can now be computed as follows:

$$\begin{aligned} \int_0^\infty d\lambda \lambda \cdot S_X \cdot F_{\lambda,0} &= \int_{\lambda_{\text{min}}}^{\lambda_{\text{max}}} d\lambda \lambda \cdot \frac{a}{\lambda^5} \cdot \frac{1}{e^{\frac{b}{\lambda}} - 1} = \\ &= a \int_{\lambda_{\text{min}}}^{\lambda_{\text{max}}} d\lambda \frac{1}{\lambda^4} \cdot \frac{1}{e^{\frac{b}{\lambda}} - 1} = \\ \left[\text{Subs. } \frac{b}{\lambda} = x \right] &= a \int_{\frac{b}{\lambda_{\text{min}}}}^{\frac{b}{\lambda_{\text{max}}}} dx \left(-\frac{b}{x^2} \right) \cdot \left(\frac{b}{x} \right)^{-4} \cdot \frac{1}{e^x - 1} = \\ &= -\frac{a}{b^3} \int_{\frac{b}{\lambda_{\text{min}}}}^{\frac{b}{\lambda_{\text{max}}}} dx \frac{x^2}{e^x - 1}. \end{aligned}$$

To solve this integral we will first solve

$$\int dx \frac{1}{e^x - 1},$$

by substituting $u = 1 - e^{-x}$. From which follows:

$$\int \frac{du}{1-u} \cdot \frac{1}{\frac{1}{1-u} - 1} = \int \frac{du}{1-u} \cdot \frac{1-u}{u} = \int du \frac{1}{u} = \ln(u).$$

By re-substituting, we find:

$$\int dx \frac{1}{e^x - 1} = \ln(1 - e^{-x}).$$

We can now solve the flux integral by applying partial integration (PI) twice

$$\begin{aligned} \int dx \frac{x^2}{e^x - 1} &\stackrel{\text{PI}}{=} \left[x^2 \cdot \ln(1 - e^{-x}) \right] - \int dx 2x \ln(1 - e^{-x}) = \\ &= -x^2 \cdot \text{Li}_1(e^{-x}) + 2 \int dx x \text{Li}_1(e^{-x}) = \\ \left[\text{Subs. } u = e^{-x} \right] &= -x^2 \cdot \text{Li}_1(e^{-x}) + 2 \int du \frac{\ln(u)}{u} \text{Li}_1(u) = \\ &\stackrel{\text{PI}}{=} -x^2 \cdot \text{Li}_1(e^{-x}) + 2 \left[\ln(u) \cdot \text{Li}_2(u) \right] \\ &\quad - 2 \int du \frac{1}{u} \text{Li}_2(u) = \\ &= -x^2 \cdot \text{Li}_1(e^{-x}) + 2 \ln(u) \cdot \text{Li}_2(u) \\ &\quad - 2 \left[\text{Li}_3(u) \right] = \\ \left[\text{Re - subs.} \right] &= -x^2 \cdot \text{Li}_1(e^{-x}) - 2x \cdot \text{Li}_2(e^{-x}) - 2\text{Li}_3(e^{-x}), \end{aligned}$$

where $\text{Li}_n(x) = \int_0^x dt \text{Li}_{n-1}(t)/t$ is the polylogarithm, with $\text{Li}_1(x) = -\ln(1-x)$. The final result can now be expressed as

$$\begin{aligned} \int_0^\infty d\lambda \lambda \cdot S_X \cdot F_{\lambda,0} &= \\ &= \frac{a}{b^3} \left[\left(\frac{b}{\lambda} \right)^2 \cdot \text{Li}_1 \left(e^{-\frac{b}{\lambda}} \right) + 2 \frac{b}{\lambda} \cdot \text{Li}_2 \left(e^{-\frac{b}{\lambda}} \right) + 2\text{Li}_3 \left(e^{-\frac{b}{\lambda}} \right) \right]_{\frac{b}{\lambda_{\text{min}}}}^{\frac{b}{\lambda_{\text{max}}}}. \end{aligned}$$

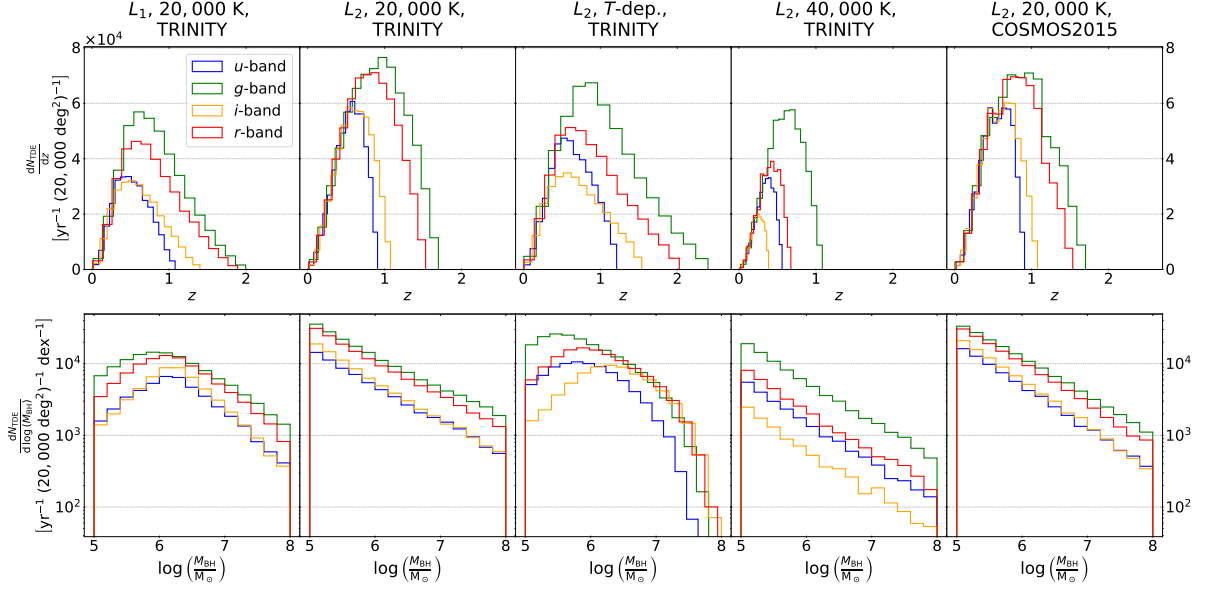


Fig. B.1: Differential rate of unlensed TDEs for five representative models. The first row shows the TDE redshift, and the second row shows the BH mass. These figures are calculated for LSST magnitude limits.

Appendix B: Unlensed TDE Distributions

In Fig. B.1, we show the expected redshift and BH mass distributions for five representative models calculated for LSST limiting magnitudes. We expect LSST to find most unlensed TDEs at $z \lesssim 1.5$. r and g -band are best suited to observe high redshift TDEs, while u and i -band only see TDEs for $z \lesssim 1$. The differential TDE rate over the BH mass follows the magnitude function. This shows clearly that the temperature-independent L_2 model prefers lower BH masses, while the L_1 and the temperature-dependent models peak around $10^6 M_\odot$.

Appendix C: Implementation

In the original implementation from Oguri & Marshall (2010), all possible lens galaxies are described by two parameters, the redshift and velocity dispersion. Hence the code calculates through a two dimensional grid. At each grid point, the number of galaxies is calculated, and for every lens galaxy, the number of possible TDEs is drawn from a Poisson distribution. As an example, when considering $20,000 \text{ deg}^2$ on the sky, we calculate above 358 billion galaxies up to a redshift of 2. Drawing 1 billion samples from a Poisson distribution takes on the order of one minute, which means a lot of time is spent on this portion of the code.

As all lens galaxies are considered the same at a given grid point, we only need to calculate the total number of possible TDEs for N galaxies. Here we can use the fact that the sum of two independent Poisson distributed variables is also Poisson distributed. Assume $X \sim \text{Poisson}(\lambda)$ and $Y \sim \text{Poisson}(\mu)$ then

$$\begin{aligned}
 P(X + Y = k) &= \sum_{i=0}^k P(X + Y = k, X = i) \\
 &= \sum_{i=0}^k P(Y = k - i, X = i) \\
 &= \sum_{i=0}^k P(Y = k - i) \cdot P(X = i) \\
 &= \sum_{i=0}^k e^{-\mu} \frac{\mu^{k-i}}{(k-i)!} \cdot e^{-\lambda} \frac{\lambda^i}{i!} \\
 &= e^{-(\mu+\lambda)} \cdot \sum_{i=0}^k \frac{\mu^{k-i}}{(k-i)!} \cdot \frac{\lambda^i}{i!} \\
 &= e^{-(\mu+\lambda)} \cdot \sum_{i=0}^k \frac{1}{k!} \frac{k!}{k!(k-i)!i!} \cdot \mu^{k-i} \cdot \lambda^i \\
 &= e^{-(\mu+\lambda)} \cdot \frac{1}{k!} \cdot \sum_{i=0}^k \binom{k}{i} \cdot \mu^{k-i} \cdot \lambda^i \\
 &= \frac{(\mu + \lambda)^k}{k!} \cdot e^{-(\mu+\lambda)}.
 \end{aligned}$$

Hence $X + Y \sim \text{Poisson}(\lambda + \mu)$. Therefore, we do not need to draw N times from a Poisson distribution but can draw from a Poisson distribution with $N \cdot \lambda$ as its expectation, significantly speeding up calculations.

Other optimizations have been made by removing the need to instantiate large data arrays not needed for this application of the code, yielding significant performance improvement without changing the code's fundamental logic. These speed increases are needed as the rate of lensed TDEs is close to or even below unity. This creates the need to over-sample the detection area by up to a factor of 1,000 to find a few samples at faint magnitudes and bring the Monte Carlo error down.

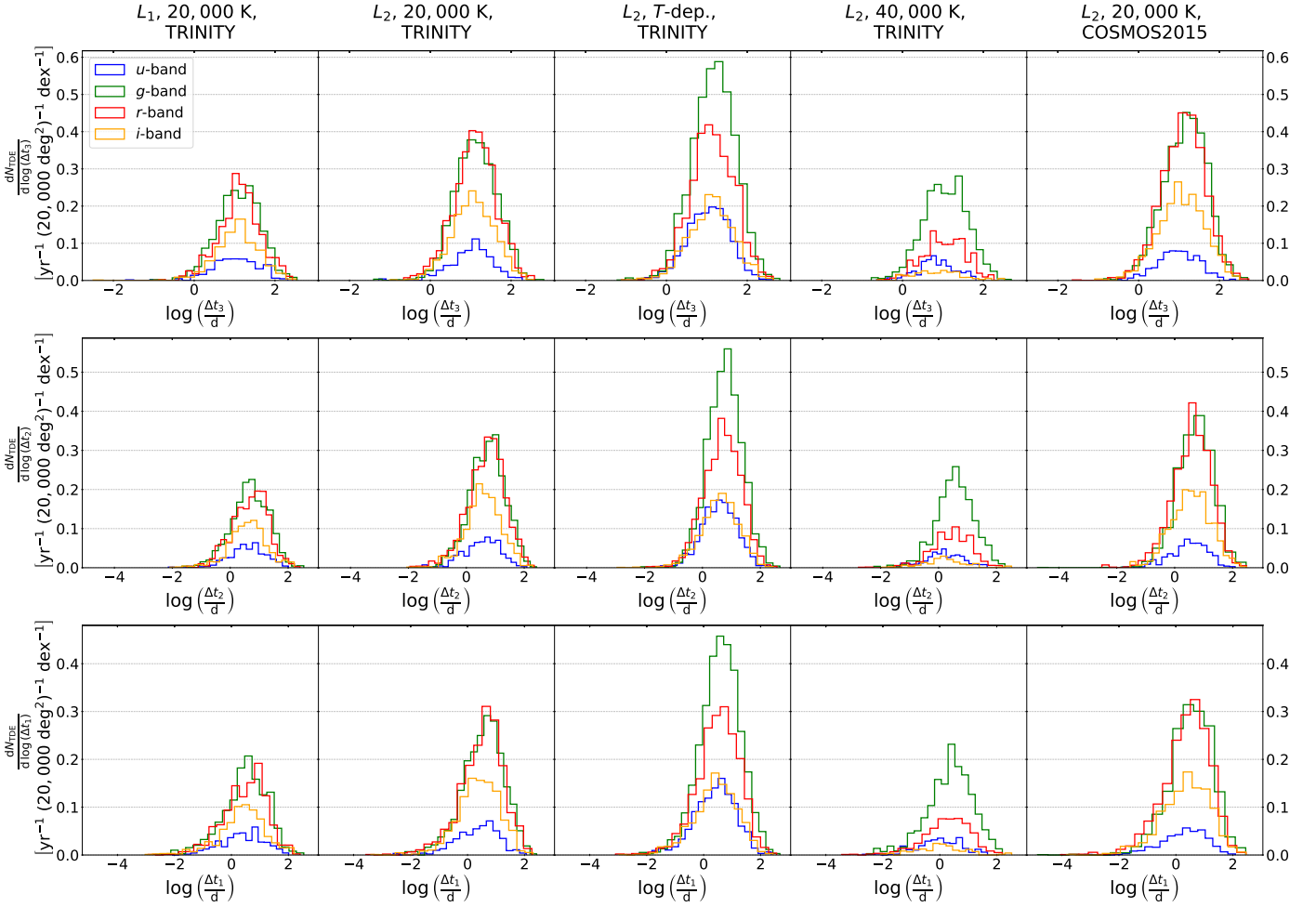


Fig. D.1: Histograms show the differential rate of TDEs for five representative models. Δt_1 is the time delay between the first and second arriving image. Δt_2 is between the first and third image. Δt_3 is the first and last image. These figures are calculated for LSST magnitude limits.

Appendix D: Quads Time Delay Distributions

In Fig. D.1, we show the time delay distributions for quad lenses calculated for LSST limiting magnitudes. The earliest image is taken as the reference image. The time delay distributions for double lenses are shown in the last row of Fig. 11. The delay between the first and second image is Δt_1 . The distributions show that we expect this time delay to be approximately 11 days. The delay between the first and third image is Δt_2 . This time delay is approximately 5 days. The delay between the first and fourth image is Δt_3 . This time delay is approximately 3 days. We find a very similar time delay distribution as for the double lenses. The quads exhibit signs of a low time delay tail that is not observed for the doubles. However, such systems seem rare and are only observed at numerical uncertainty.